High power tests of a remote steering antenna at 140 GHz

B. Plaum[1], G. Gantenbein[1], W. Kasparek[1], K. Schwörer[1], M. Grünert[1], H. Braune[2],
V. Erckmann[2], F. Hollmann[2], L. Jonitz[2], H. Laqua[2], G. Michel[2], F. Noke[2], F. Purps[2],
A. Bruschi[3], S. Cirant[3], F. Gandini[3], A.G.A. Verhoeven[4], ECRH groups at
IPP Greifswald[2], FZK Karlsruhe[5] and IPF Stuttgart[1],

[1]Institut für Plasmaforschung, Universität Stuttgart, Pfaffenwaldring 31, D-70569 Stuttgart, Germany
[2]Max-Planck-Institut für Plasmaphysik (IPP), EURATOM-Association, D-17491 Greifswald, Germany
[3]Instituto di Fisica del Plasma, EURATOM-ENEA-CNR Association, via R Cozzi 53, 20125 Milano, Italy
[4]FOM Institute for Plasma Physics Rijnhuizen, Association EURATOM-FOM, Nieuwegein, The Netherlands
[5]Forschungszentrum Karlsruhe, Association EURATOM-FZK, IHM, D-76021 Karlsruhe, Germany
e-mail: plaum@ipf.uni-stuttgart.de

Abstract

This paper reports the results of the high-power test of a remote steering launcher mock-up at 140 GHz, which were performed at the ECRH installation for the future stellarator W7-X at IPP Greifswald. The mock-up test system consists of a 6.62 m long square corrugated waveguide with a steerable optic at the entrance and various diagnostics at the exit of the waveguide. A straight launcher and version with 2 integrated mitre-bends were investigated.

The high-power tests of the straight setup have been performed with powers up to $P_0 = 700$ kW (typically 500 kW) and pulse lengths of up to 10 seconds. In the dog-leg verison, arcing limited the power and pulse length.

For both polarizations (parallel and perpendicular to the steering plane), no arcing was observed within this range of power and pulse-length for the straight setup, in spite of the fact, that the experiments were performed under ambient atmospheric conditions. After the integration of 2 mitre bends in the setup, arcing limited the usable parameter range. The ohmic loss P_Ω of the waveguide was measured via the temperature increase of the waveguide wall, and was used to calibrate the calculated angular dependence of the total ohmic losses of the waveguide. Short-pulse radiation pattern measurements with thermographic recording show high beam quality and confirm the steering range of $-12° < \phi < 12°$. The version with two mitre bends produces similar results but with an increased level of sidelobes and arcing problems.

1 Introduction

The International Thermonuclear Experimental Reactor (ITER) will be equipped with an electron cyclotron resonance heating (ECRH) system which can be applied for very localised heating of the plasma or for current drive (ECCD) in the plasma [1]. One major objective of this system is the suppression of plasma instabilities, in particular the so-called neoclassical tearing modes (NTMs) which are very likely to appear in current operating

scenarios of ITER. The upper launcher concept under investigation, which is foreseen to fulfill this task, is the so-called remote steering launcher. Its main technical advantage is that movable parts close to the plasma are completely avoided while the injection angle of the beam into the plasma is adjusted several meters away from the plasma. The launcher basically consists of a square corrugated waveguide with a steerable mirror at the entrance of the guide [2]. Owing to the imaging properties of the guide [3], the steering at the input is transformed to the output of the waveguide if the length L is $4a^2/\lambda$ where a is the transversal dimension of the square waveguide and λ is the free space wavelength. Thus, beam steering without movable parts near to the plasma is possible.

At present, the upper launcher is designed by a consortium of European research institutes [4], and various tests will be performed after manufacture of a prototype launcher. As an intermediate step, low-power [2] as well as high-power tests of a mock-up were performed. This paper reports the results of the high-power test of a remote steering launcher mock-up at 140 GHz, which were performed using the ECRH installation of the future stellarator W7-X. For this device under construction at IPP Greifswald, a 140 GHz, 10 MW CW ECRH system is presently being installed [5]. The RF power will be delivered by 10 gyrotrons. Prototype gyrotrons were developed in Europe (Forschungszentrum Karlsruhe (FZK) in collaboration with several other research institutes and Thales Company as the industrial partner [6]) and USA (CPI). At IPP Greifswald, the first gyrotron "Maquette" became operational at the end of 2003 and is operated routinely with pulses up to 800 kW. This tube was used for the mock-up tests.

The millimetre waves are transmitted from the source to the plasma via quasi-optical transmission lines [7]. The mirrors and other components are placed in an underground duct connecting the gyrotron building with the stellarator hall. The RS-launcher mock-up experiments were performed in this underground duct, as it provides an ideal test bed for high-power experiments under atmospheric conditions.

2 Design of the beam-line mock-up for tests at 140 GHz

The basic experimental set up in the underground duct connecting the gyrotron hall and the W7-X hall is shown in Figs. 1 - 3.

For the tests of the upper launcher mock-up, the beam from the Maquette gyrotron is detoured in front of the dummy load by a fixed beam shaping mirror and a rotatable mirror and directed into the square corrugated waveguide as shown in Fig. 1 (left). The aluminium waveguide with a cross-section of 60 ×60 mm and a length of 6.62 m is mounted on a stable frame construction. The beam shaping mirror M_B (see detail in Fig. 1 right) is used to match the incident beam to the diameter of the square waveguide. The rotatable mirror M_S is mounted on a remotely controlled turntable and determines the steering angle of the launcher. It is equipped with a polarization sensitive directional coupler to check the polarization of the input beam set by polarizers. The steering plane is horizontal.

At the entrance and the exit of the waveguide, arc detectors are installed. Near to the entrance of the waveguide, an array of thermal sensors is installed to measure temperatures
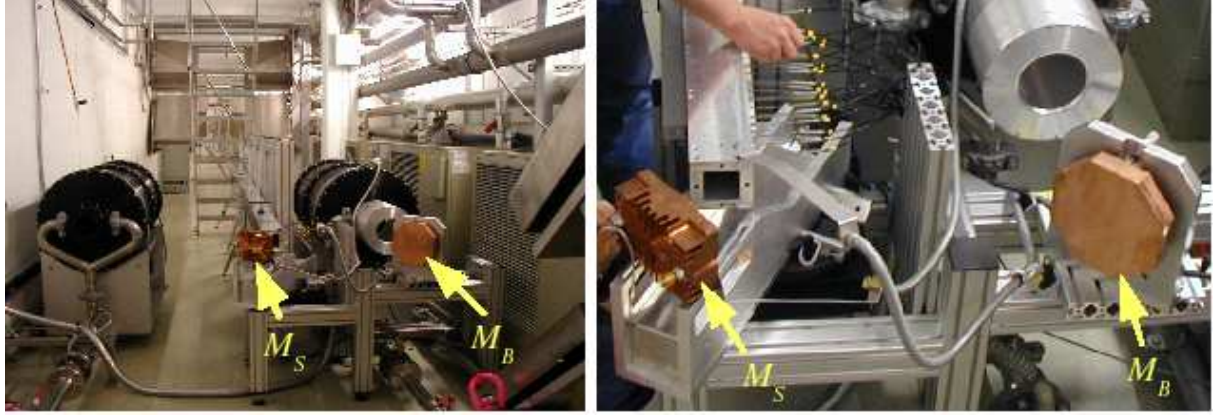
Figure 1: Left: Set up for the high-power test of the launcher mock-up consisting of the beam matching mirror M_B, the steering mirror M_S mounted on a turntable and the square waveguide. Right: Detailed view of the input optics and diagnostics
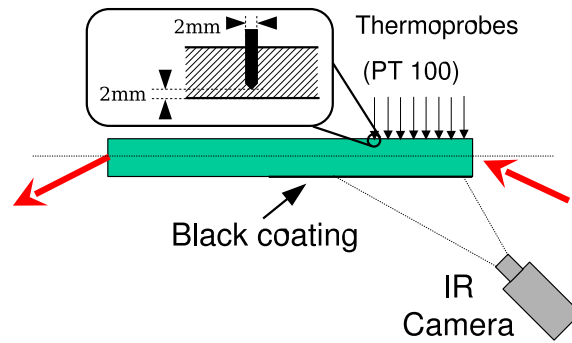

Figure 2: Experimental setup for measuring the temperature increase of the waveguide walls

in the waveguide (See Fig. 2). The opposite waveguide wall is coated with an IR absorbing surface to detect the surface temperature distribution of the waveguide (see Fig. 2). At the output of the waveguide, a long-pulse calorimetric load from CNR/IFP Milano [8] (Fig. 3) is installed to dump and to measure the transmitted power for long-pulse experiments; alternatively, an absorbing screen can be set up to record the radiation pattern of the launcher with an infrared camera.

3   Reference measurements

3.1   Characterization of the input beam

Prior to the experiments, the input beam to the experimental set up was characterized. The beam power distribution was measured using thermographic techniques at several positions in front of the CCR load (with the beam shaping mirror being removed). A typical pattern is plotted in Fig. 4a, showing high TEM_{00} mode purity. The beam patterns were analysed (symbols in Fig. 4b), and from a fit of the beam radii to the calculated Gaussian beams (lines in Fig. 4b), the beam parameters of the input beam were obtained. As can be seen from the figure, the beam is nearly axisymmetric and coincides closely with the beam as foreseen for the tests of the launcher mock-up (dotted line in Fig 4b). Therefore, the beam shaping mirror was only slightly remachined such that the input beam to the waveguide was completely axisymmetric with parameters corresponding to the horizontal beam contour as given in Fig. 4b. This resulted in a beam waist of 17 mm and an average position of the waist of about 50 mm inside the waveguide. This small deviation from the design value is negligible, as the Rayleigh-length of the beam of 424 mm is large compared to this offset.

3.2   Polarization of the test beam

As all tests were performed with parallel and perpendicular polarization with respect to the steering plane, the polarization of the input radiation as function of the polarizer settings was checked prior to the experiments using a polarization sensitive coupler integrated into the steering mirror. For both polarization planes, the tests yielded a linear polarized beam with a maximum cross-polarized component of 3 %.

3.3   Position of the input beam

The positions and orientations of the steering mirror, the axis of the turn-table and the waveguide entrance had been chosen such that the beam enters the waveguide aperture in its centre for all steering angles. To confirm the input geometry, the beam position of the input beam was checked by thermographic recording of the beam with a target on the waveguide entrance. Within the measurement accuracy of about 3 mm, no significant deviation from the ideal beam position could be detected.
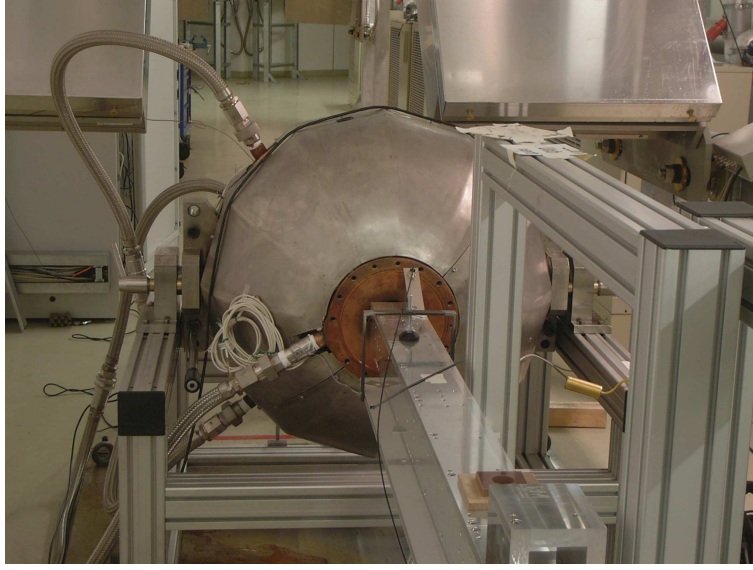
Figure 3: Calorimetric long-pulse load built by IFP Milano. It consists of a water-cooled absorbing sphere and an optimized conical reflector opposite to the entrance of the load to distribute the power over the absorbing surface. The load is installed at the exit of the launcher mock-up on a rotatable carriage to allow adjustment according to the steering angle.
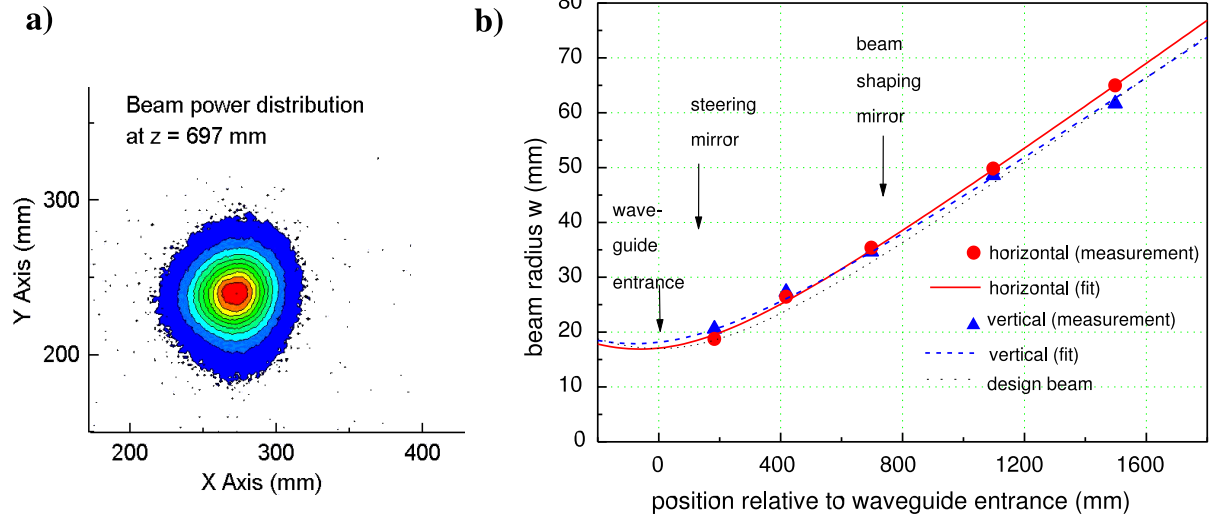

Figure 4: a) Power distribution of the Gaussian beam at $z = 697$ mm. The colour steps correspond to equal steps in power, the dynamic range shown is 17 dB.
b) Waist radii in horizontal (measurement: dots, fit: solid curve) and vertical (measurement: triangles, fit: dashed) direction of the beam incident to the beam shaping mirror M_B. With M_S, the beam is circular with the parameters corresponding to the solid curve. For reference, the design beam for the launcher mock-up test is shown as dotted curve.

5

4 Temperature increase of the waveguide wall

4.1 Theory

The most simple approximation of the fields in the waveguide is the assumption of a Gaussian beam which propagates along a zig-zag line in the waveguide. If one knows the absorption of a single reflection at the wall, the total losses and the heat load can be estimated by calculating the number of reflections from the steering angle and the waveguide dimensions.
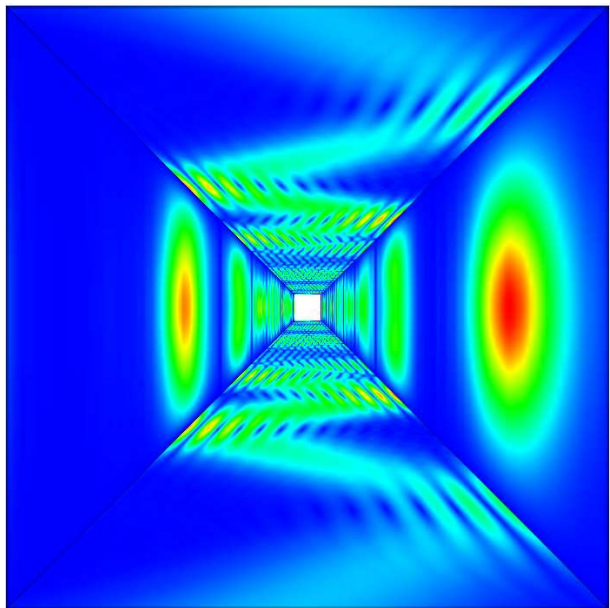

Figure 5: 3D View into the waveguide entrance with the calculated wall current distribution for a steering angle of 11.6°. The steering plane is horizontal, the scale of the wall currents at the left and right wall is different from the scale of the top and bottom wall, where the wall currents are much lower.

A more precise calulation of the field structure involves the expansion of the incoming Gaussian field into hybrid modes of the corrugated waveguide [9]. Once the complex mode amplitudes at the entrance of the waveguide are obtained, the modes can be propagated in the waveguide with known phase constants. A superposition of the mode fields allow the calculation of all field components at arbitrary waveguide positions.

For estimating the losses, the longitudinal component of the H-Field at the walls is of interest, because it corresponds to a wall current in transversal direction, which is the main cause of the loss. A calculated pattern of the transversal wall currents is shown in Fig. 5. One can see, that at the beginning, the beam looks nearly Gaussian. Further inside the waveguide however, the pattern no longer consists of distinct reflections due to the relative phase shift of the modes resulting from the different phase constants.

At the output, the input field is reconstructed antisymmetrically if the length is chosen properly. In this case the overall field pattern is approximately symmetrical to the transversal plane at $z = L/2$. This results in a last reflection near the end of the waveguide, which is again similar to a reflected Gaussian beam.

The estimation based on zig-zag propagation however, was found to be in reasonable agreement with the more precise calculation using the mode analysis method.

4.2 Resonator measurements of the absorption coefficient for a corrugated waveguide wall

Prior to the high-power tests of the corrugated waveguide, a part of the wall was characterized in a 3-mirror resonator set-up [10]. Using this technique, the absorption coefficient
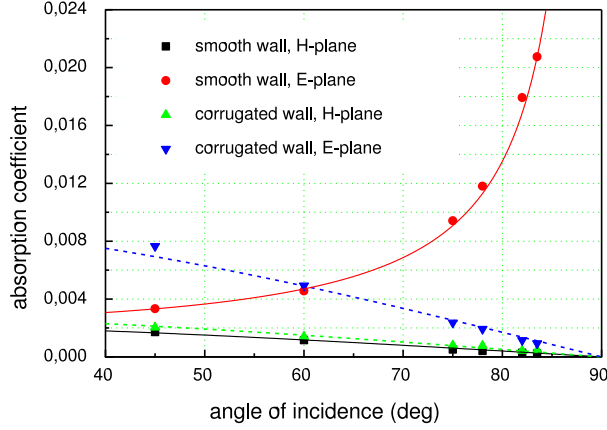
Figure 6: Absorption coefficient at 158 GHz for a Gaussian beam reflected from the corrugated aluminium wall of the remote steering waveguide for parallel and perpendicular polarization, respectively. For reference, the absorption coefficients for a plane aluminium plate are plotted as well. Symbols: Measurements with 3-mirror resonator. Lines: Fit to measured data

as function of polarization and angle of incidence could be measured. Note that this measurement models the conditions for the first bounce of the input beam on the wall of the corrugated waveguide. The results performed over a wide angular range are shown in Fig 6. For reference, also absorption coefficients of a plane surface are plotted, which agree well with theory except for a typical enhancement factor of about 1.4 due to surface roughness. The absorption coefficients for the corrugated wall can be fitted by

$$a_\parallel = 0.0098 \cos\alpha = 0.0098 \sin\phi \text{ (E-Plane)} \tag{1}$$

$$a_\perp = 0.0030 \cos\alpha = 0.0030 \sin\phi \text{ (H-Plane)} \tag{2}$$

Here, α is the angle of incidence, which is given by $\alpha = 90° - \phi$. One can see, that in the corrugated case a similar dependence is obtained for both polarisations. However, losses in the E-Plane (which corresponds to the plane with polarisation parallel to the steering plane) are about three times higher than in H-plane. Note especially the huge difference between the corrugated and the plane surface for E-plane at large angles of incidence (small steering angles), which is the reason for efficient propagation of low-order HE_{mn} modes. The results obtained above can be used to calibrate the calculations in 4.1. Moreover, they can be scaled to other conditions like those in the RS launcher for ITER (see chapter 8.2).

4.3   Setup for the temperature measurements

For measuring the temperature increase of the waveguide wall with an IR-camera, the outer wall was coated with black self adhesive plastic foil to improve the radiation characteristics. On the opposite side, thermocouples were attached in holes of the wall to measure the temperature near the inner wall (see Fig. 2).

4.4 Heat distribution at the outer waveguide wall

The measurements were done with powers up to 700 kW and pulse lengths of up to 10 s. Fig. 7a shows the heat distribution at the outer waveguide wall for a steering angle of 11.6°, which is close to maximum angle of 12° up to which the antenna can be used. One can see the 2nd and 4th reflection of the beam. The trapezoidal deformation of the image was numerically compensated, the rectified image is shown in Fig. 7b. The calculated wall current density is shown in Fig. 7c. One can see, that a good agreement of measurement and calculation was achieved.
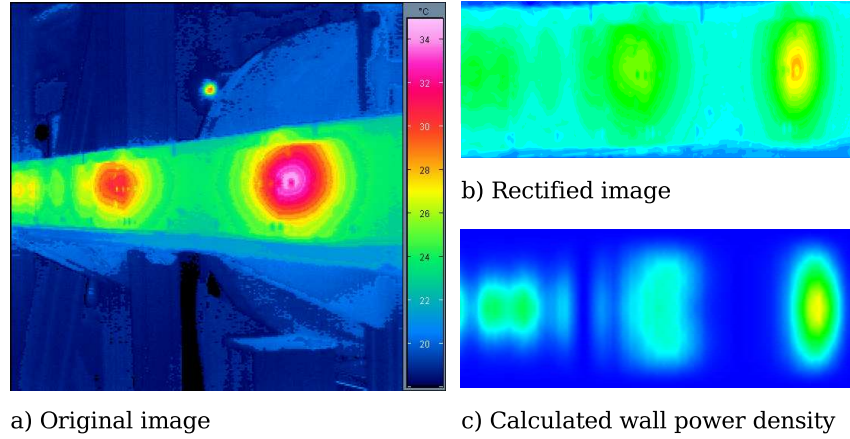

a) Original image

b) Rectified image

c) Calculated wall power density

Figure 7: Thermographic image of the waveguide wall ($\phi = 11.6°$, $P \approx 500$ kW, Pulse length: 8 s, Parallel polarization)

4.5 Estimation of the absorption coefficient for one reflection

The temperature values near the inner waveguide wall, which were detected by the thermocouples, were used to extrapolate the power loss due to the first reflection of the beam at the waveguide wall.

The thermocouples were arranged in 3 rows parallel to the waveguide axis. The temperature values of the thermocouples were recorded, the results for the middle row, where the temperature increase is the highest, are shown as an example in Fig. 8. For the sensors in the center of the reflection spot, the temperature increases during the pulse followed by a cooling phase. Other areas are mainly heated by transversal heat diffusion resulting in a monotonous increase within the observed time interval.

The peak temperatures at the end of the pulse were used to calculate the heat energy content in the waveguide wall. This was achieved by assuming Gaussian temperature profiles in both the transversal and longitudinal direction. This profile was fitted to the measured values (See Figs. 9 and 10).

In addition, the temperature was assumed to be constant from the inside to the outside of the wall, i.e. the thermal conductivity was assumed to be infinite in this direction. The resulting heat distribution (See Fig. 10) could be used to calculate the heat energy content of the wall and thus the total heat power due to one reflection. For a steering angle of 11.6°, the resulting power losses for the first reflection are 0.9 kW (0.18 %) and
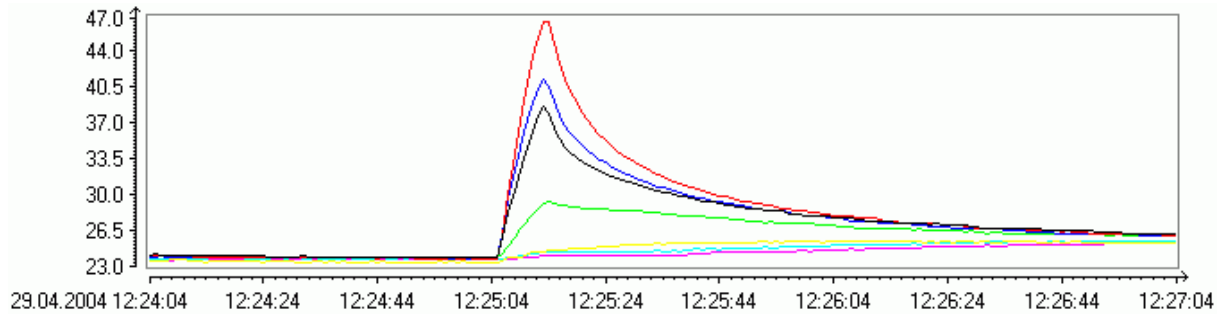
Figure 8: Temperature values at the middle row for 8 s, $P \approx 500$ kW, $\phi = 11.6°$, parallel polarization
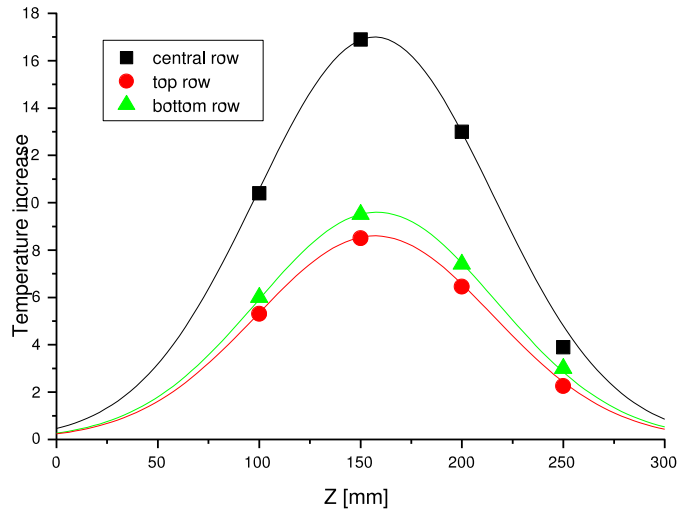

Figure 9: Gaussian fit to the measured temperature profiles

0.3 kW (0.06 %) for parallel and perpendicular polarization respectively for a gyrotron power of 500 kW.

4.6   Estimation of the total ohmic losses

The overall efficiency directly could not be measured directly, because there was no reliable possibility for monitoring the power at the input of the waveguide.

One can, however, calculate the wall current distribution at the inner waveguide walls (See Fig. 5). The wall current corresponds to the ohmic losses ($P_{loss} \propto |I_{wall}|^2$) but the proportionality factor cannot easily be derived, because it depends on the complicated field distribution inside the corrugation grooves. From the current distribution, however, one can calculate the loss of the first reflection normalized to the total loss. For a steering angle of 11.6°, this ratio is 0.0438. This results in total losses of 4.1 % for parallel polarization and 1.36 % for perpendicular polarization.

For comparison, Fig. 11 summarises the results obtained from low- and high-power measurements. Fig. 11 shows the absorption coefficients as function of the steering angle. From this, the overall losses of the launcher under ITER conditions for parallel and perpendicular polarizations can be estimated by the formulas
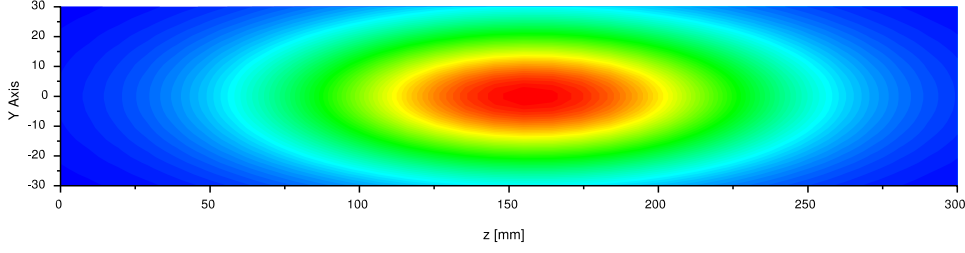
9

Figure 10: Fitted 2D temperature profile

$$P_{\Omega,\parallel}/P_0 = 0.033\phi^2[°, \%]$$

$$P_{\Omega,\perp}/P_0 = 0.01\phi^2[°, \%].$$

These formulas are derived from the data by integration of the wall currents over the side walls of the waveguide under the assumption, that the contribution of the walls parallel to the steering plane is negligible. Note that the measurements were taken at different frequencies of 158 GHz (low-power) and 140 GHz (high-power) and cannot be compared directly. However, the error from this difference due to difference in conductivity and relative corrugation depth is estimated to be $\leq 6\%$; in view of the large error bar of the high-power data, the frequency difference is negligible and a correction was not performed. Within the error bars, a good agreement between the low- and high-power measurements is found. The solid and dashed lines are taken from the fit to the resonator data over the whole angular range. The reason for the small systematic deviation of the data in the angular range relevant for remote steering could not be clarified yet.

5 Far-field measurements

The far-field measurements were carried out by placing an absorbing screen at a distance of 2.175 m from the waveguide output and recording the field pattern with an IR camera. Due to the limited space, the distance of the screen from the waveguide output could not be freely chosen. For safety reasons, a temperature rise of no more than 10°C (as shown by the camera) was allowed. The gyrotron was operated at a power of about 250 kW, the pulse length was 0.3 ms. These parameters correspond to the lowest possible pulse energy, at which the gyrotron operates reliably.
Fig. 12 shows the far-field pattern for parallel polarization at a steering angle of 10°. The upper picture shows the high-power measurement, the lower picture shows the corresponding low-power measurement. The temperature increase of 10°C corresponds to a dynamic range of 20 dB, which is much lower than for the low-power measurements, which were performed with a vector network analyzer and have a typical dynamic range of at least 40 dB. Thus, the sidelobes, which are visible in the lower image do not show up in the upper image.
Fig. 13 shows high- and low-power measurements for parallel polarization at a steering angle of 15°. At this angle, the conditions for the imaging properties of the waveguide are
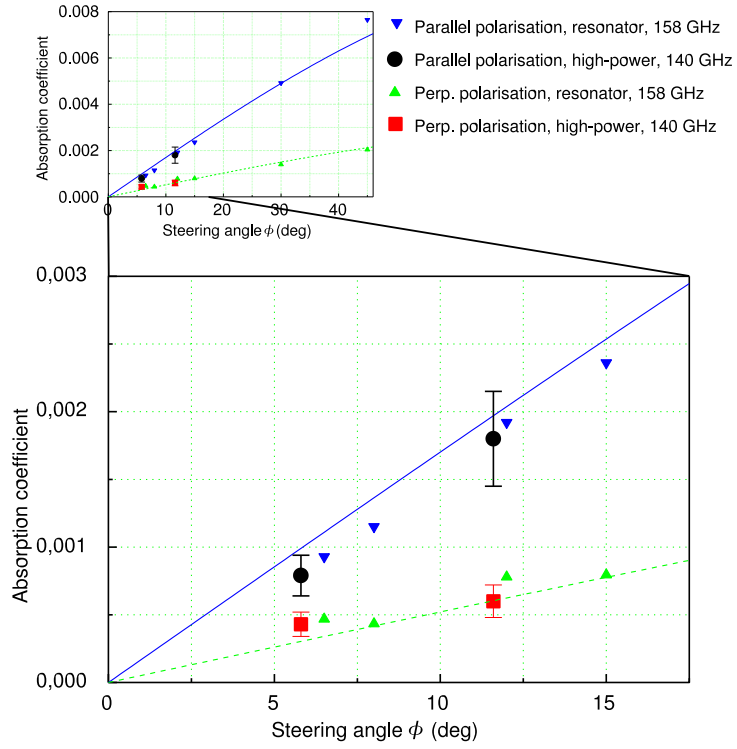
Figure 11: Comparison of the absorption coefficients for the corrugated waveguide wall measured with low-power (up- and down-triangles) and high-power (dots and squares). The solid and dotted curves are fits to the low-power data for parallel and perpendicular polarization, respectively. The upper diagram shows the whole angular range ($6.5° \leq \phi \leq 45°$) of the low power measurements, the lower diagram shows the range where the high power measurements were performed.

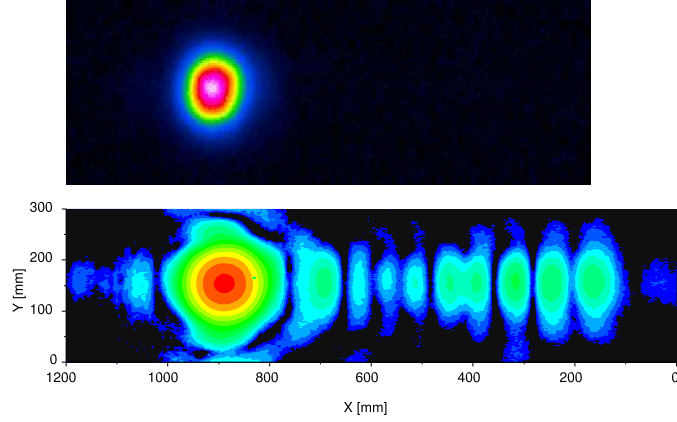no longer fulfilled and one observes a splitting of the output beam.

Figure 12: Far-field patterns for a steering angle of 10° (parallel polarization). Top: High power measurement at a distance of 2.175 m (linear temperature scale), Bottom: Low-power measurement at a distance of 1.7 m (logarithmic scale, 3 dB / color step)
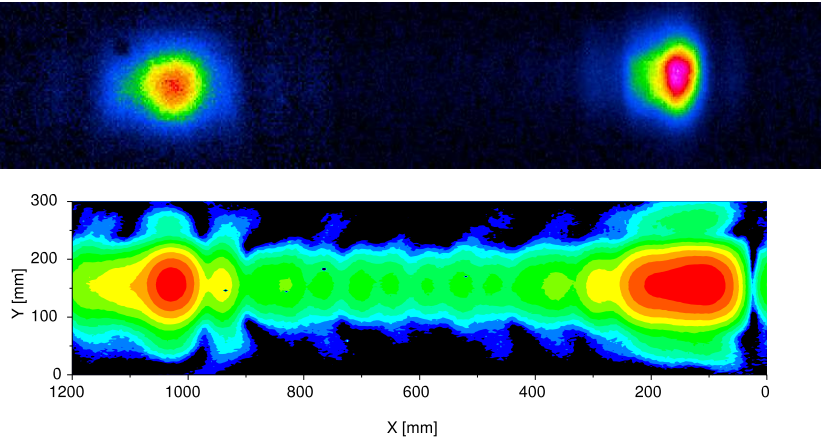

Figure 13: Far-field patterns for a steering angle of 15° (parallel polarization). Top: High power measurement at a distance of 2.175 m (linear temperature scale), Bottom: Low-power measurement at a distance of 1.7 m (logarithmic scale, 3 dB / color step)

Fig. 14 shows a summary of far-field patterns for both polarizations and all steering angles. For steering angles up to 12°, the patterns look nearly identical. This indicates, that the antenna can also be used for elliptically polarized beams, which are necessary for ECCD. At a steering angle of 15°, the patterns for both polarizations differ slightly. This is due to the fact, that the corrugation is not perfectly matched for 140 GHz resulting in slightly different phase constants for higher-order modes. Earlier low-power experiments showed, that the antenna with the current corrugation profile is completely polarization independent at a frequency of 158 GHz.
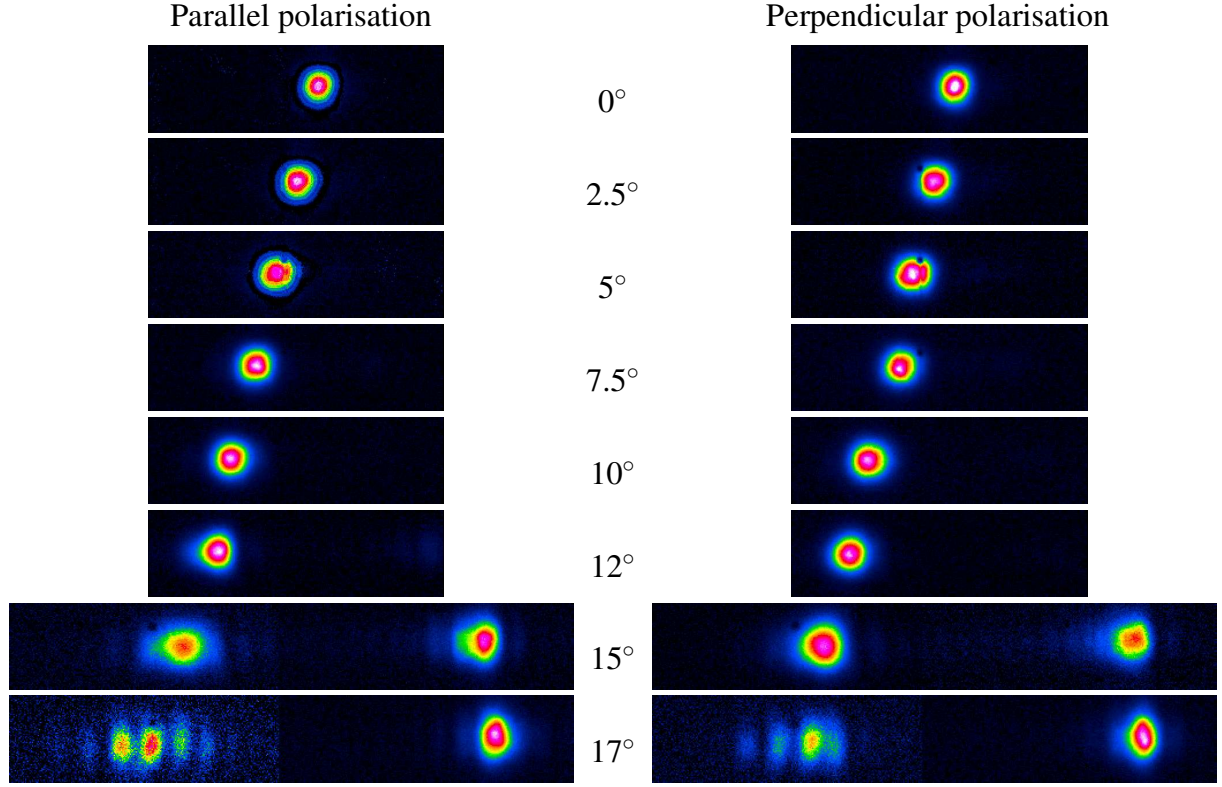
Parallel polarisation   Perpendicular polarisation

Figure 14: Far field patterns at a distance of 2.175 m from the waveguide output for parallel (left) and perpendicular (right) polarization

6 Breakdown limits

Arc detectors were used at the input and output of the straight waveguide to explore the breakdown limit of the mock-up. For the setup without mitre bends, no limitation due to arcing in the square waveguide was found. In Table 1, typical parameters of the shots performed are listed.

t [s]	P [kW]	ϕ [°]	Polarization	Remarks
10	500	11.6	Perp.	Typical parameters for monitoring the
10	500	9.0	Parallel	temperature increase of the waveguide wall
1	700	11.6	Perp.	
0.2	800	11.6	Perp.	Pulse length limited by gyrotron
0.0003	250	20.0	Parallel	Far-field measurement

Table 1: The parameter space (pulse length t, power P and steering angle ϕ) were the waveguide has been operated without observing a limitation due to arcing in the waveguide. The polarization is given with respect to the steering plane. For monitoring the temperature increase of the waveguide wall, the gyrotron has been operated in a reliable and reproducible regime. In the case of far-field measurements, the pulse length and power was reduced in order to avoid damaging the absorber material.

7 Integration of mitre bends

7.1 Setup

For ITER, mitre bends are possibly needed in the remote steering antenna to reduce the neutron flux to the window. Therefore, the straight waveguide set up was modified by inserting two 90° bends (3.1 m straight - 90° bend - 0.28 m straight - 90° bend - 3.24 m straight, see Fig. 15). Thus, the length of the complete waveguide run was 6.62 m, i.e., nearly identical to the straight set up. Input beam and steering system were kept unchanged.

Mitre bends enhance the ohmic and diffraction loss in the square waveguide. For minimum ohmic loss of the mitre bends (typically 0.1% in H-plane, 0.2% in E-plane), the mirrors were made from 20 mm thick copper, with two holes each for connection of arc detectors. Diffraction in the plane of the bends occurs in the region where the waveguide wall is interrupted. The corresponding loss depends on the field structure in the region of the mitre bends, i.e., on the position of the bends within the waveguide and the beam waist radius at the input of the waveguide [2]. Theory [12] claims that mode conversion in this plane is negligible, i.e. less than 0.5% depending on the input beam, provided that the bends are positioned in the middle between input and output. This was taken into account (see above).
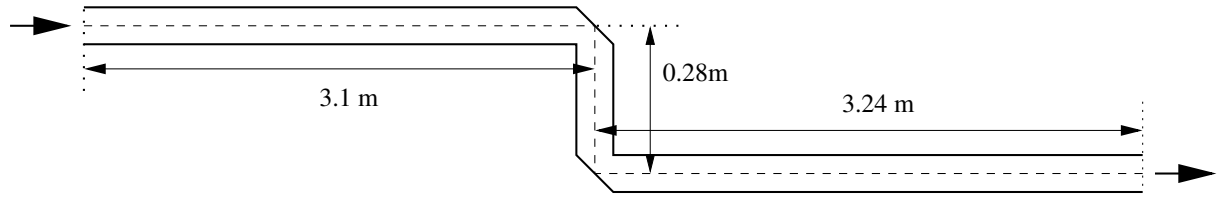

Figure 15: Setup of the waveguide with mitre bends

Diffraction loss in the plane perpendicular to the mitre bends occurs due to the abrupt change of the direction of the corrugations and the resulting wrong boundary conditions in the wall of the bends. In a previous study, relative high loss (several percent) was found for standard bends, therefore a programme to optimize the mitre bends was started [2]. In the present test, mitre bends with an optimized corrugation were used. These bends employ corrugations rotated by +45° (corrugations parallel to the mitre bend mirror, see Fig. 16) in the triangular area, where both the incident and the reflected waves propagate. To achieve optimal boundary conditions for rotated corrugations, the corrugation depth was matched to the rotation angle β relative to the original orientation with

$$d(\beta) = (1 - \cos^2 \phi \sin^2 \beta)^{-0.5} d(0°) \tag{3}$$

(cf. also [13]), which resulted in a depth of $d = 0.62$ mm.

7.2 Radiation patterns

Corresponding to the tests of the straight waveguide, radiation patterns were recorded by thermographic imaging. For these measurements, a wide-angle lens (f=12.5 mm) could
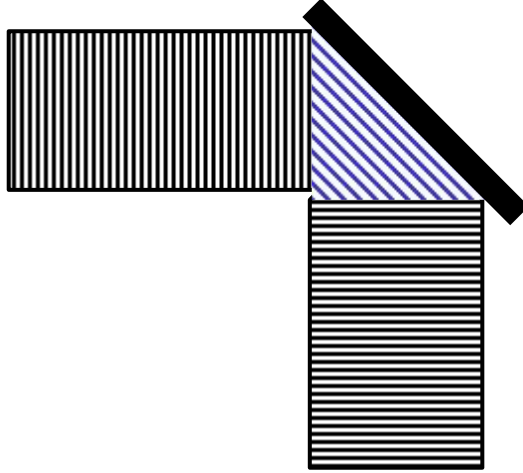
Figure 16: Corrugations in the side wall of the improved mitre bends.

be used in the infrared camera, which resulted in a larger field of view. Again, the system was tested with both polarizations. Fig. 17 shows the radiation patterns in the range $-15° \leq \phi \leq 17.5°$ for polarization parallel to the steering plane. One can see, that the steering range of $-12° < \phi < 12°$ is identical to the straight launcher. However, side lobes opposite to the main beam with a level of -21 dB...-17 dB with respect of the main lobe can be seen. These side lobes are mainly the result of diffraction at the non-perfect wall of the mitre bends. The figure also confirms the splitting of the beam at $\phi \approx 15°$ and the revival of the main lobe on the opposite side at $\phi \approx 17.5°$. In order to get an estimate on the diffraction loss, the power in the main lobe was deduced from the thermographic images and related to the total radiated power within the field of view of the camera. This power is assumed to be identical to the total power, as no significant lobes are expected outside of the area detected by the camera. Fig. 18 shows the relative power in the main beam (dots) evaluated by this technique. Within the nominal steering range, the efficiency is at least 86%. The solid line is a result from a corresponding low-power measurement, where 4% diffraction loss at $\phi = 0°$ have been assumed. For this case a good agreement is obtained. For the polarization perpendicular to the steering plane, no remarkable differences compared to the polarization parallel to the steering plane where found.

7.3 Long-pulse test, arcing problems

In contrast to the straight set up, arcing often occurred in the region of the mitre bends. For short pulses (typ. 1 ms), operation at power levels around 500 kW was possible in the polarization parallel to the steering plane. In the perpendicular polarization, arcing occurred earlier even for small angles. This can be explained by field enhancement at the sharp edges of the mitre bends for the polarization perpendicular to these edges, i.e., perpendicular to the steering plane. Long-pulse experiments were performed at steering angles of $\phi = 0°$ and $\phi = 10.8°$ with powers up to 500 kW and pulse lengths up to 5 s. At $\phi = 0°$, arc-free operation was possible at 500 kW in parallel polarization and up to
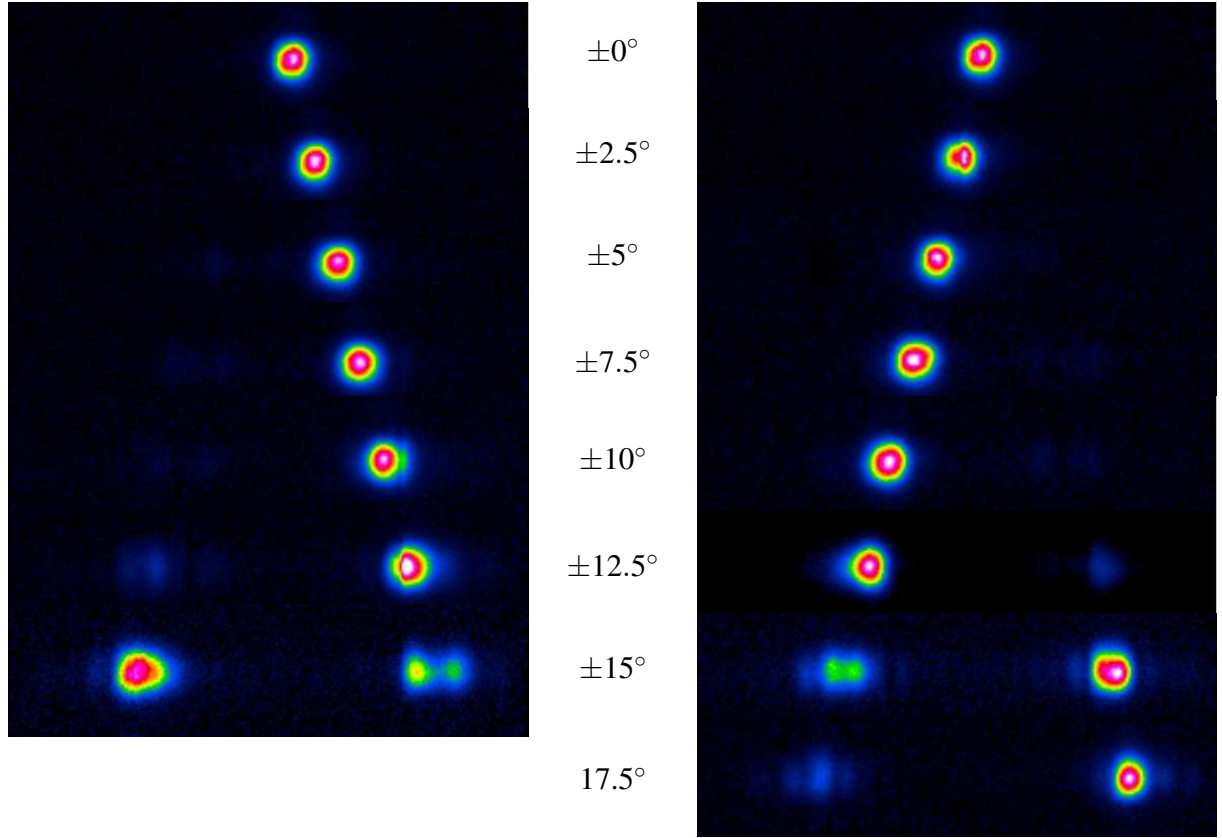
15

Figure 17: Radiation patterns of the antenna with 2 optimized mitre bends for $-15° \leq \phi \leq 17.5°$ (Polarization parallel to the steering plane)

about 300 kW in the perpendicular polarization. For $\phi \approx 10°$, arc-free operation was difficult to achieve even with moderate power. Here, only periodic pulses (10 ms, duty cycle 0.5) could be transmitted. A summary of the arcing limits is given in Table 2. It should be noted, that determining precise arcing limits is not easy because after one arc, the air inside the waveguide is polluted which results in a lower breakdown field strength for subsequent pulses.

Angle	Par. pol.	Perp. pol
0°	no arcs	1.4 ms @ 500 kW
2.5°	no arcs	no arcs
5°	1.4 ms @ 600 kW	10 ms @ 500 kW
7.5°	no arcs	4 ms @ 500 kW
10°	no arcs	2 ms @ 500 kW
12.5°	1.5 ms @ 450 kW	1 ms @ 500 kW

Table 2: Arcs observed in the waveguide with 2 mitre bends. The time values are the pulse durations, after which the arc occurred.
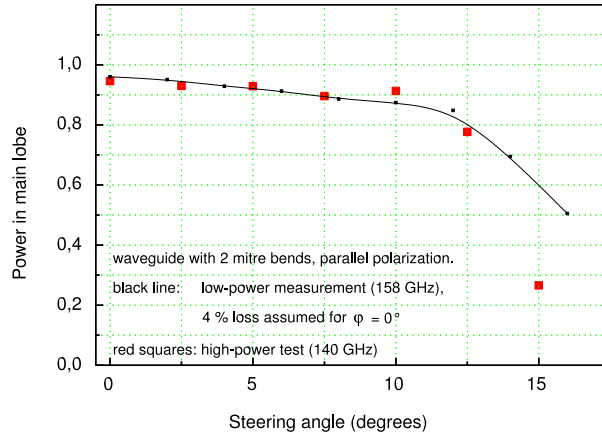
16

Figure 18: Power in the main lobe for the RS-launcher with 2 mitre bends

7.4 Temperature increase at the mitre bends

The temperature patterns near the input and output of the waveguide look quite similar for both the straight setup and the setup with mitre bends. Additional experiments were done to obtain the temperature increase in the area of the mitre bends. Fig. 19 shows a temperature image for $\phi \approx 10°$. The peak temperature in the area of the rotated corrugation (between the locations A and B for the first bend and C and D for the second bend) is 3 times higher than the peak temperature at the first reflection point near the waveguide input.
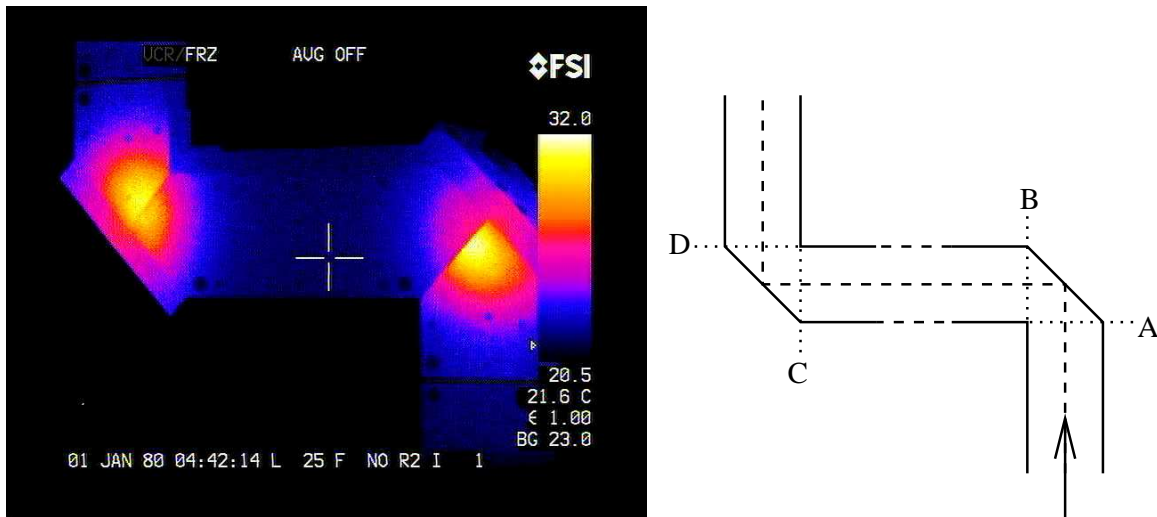

Figure 19: Temperature increase and locations of the 45° corrugation

Fig. 20 shows the calculated wall current density for the first 5 meters of the antenna. The locations A, B, C and D correspond to Fig. 19. One can see, that the wall fields are very low in the middle between the mitre bends. In the neighboring areas, however, there are regions with high field strengths, which are positioned near the rotated corrugation. In conjunction with a higher wall absorption in the area of the 45° corrugation, these
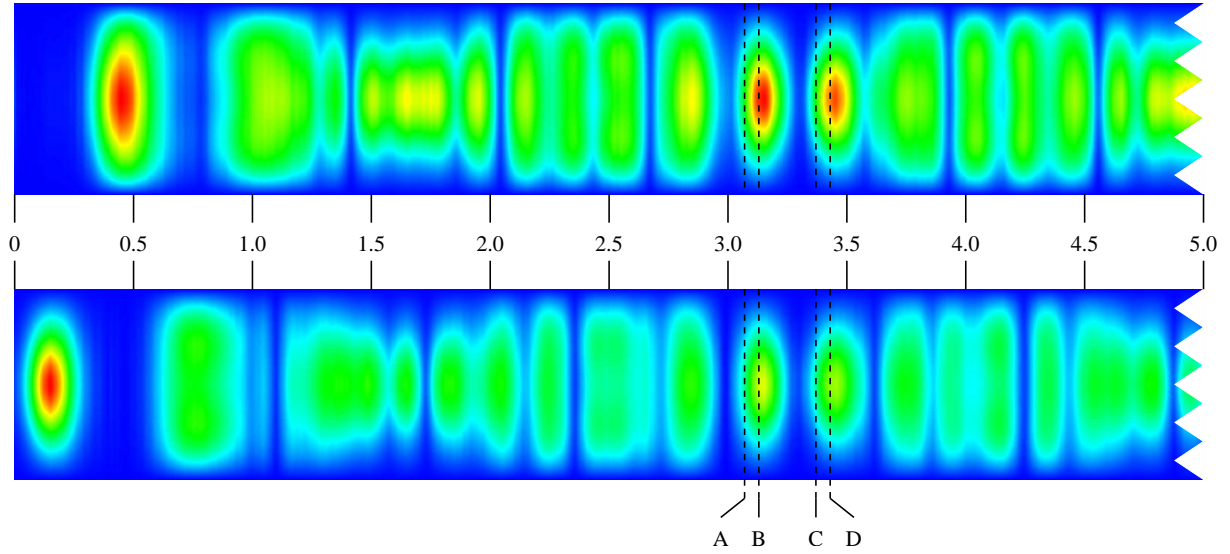
17

Figure 20: Calculated wall current density and locations of the the mitre bends. Top: left wall, Bottom: right wall

explain the high losses. These results can be used to optimize the locations of the mitre bends in future applications.

8 Consequences for the application on ITER at 170 GHz

In the following, some consequences as well as possible improvements for the application on ITER at 170 GHz are discussed. It is assumed, that the waveguide consists of pure copper and is operated at a surface temperature of 200°C. The waveguide cross-section is quadratic with $a = 44$ mm, the length is taken as $L = 4.33$ m. The power at the waveguide entrance is 2 MW.

8.1 Input beam and radiation patterns

No principle differences between the measured radiation patterns and the expected ones for the ITER RS launcher (before the front optics) are expected. Note that for similar input beam conditions, the beam divergence scales with λ/a, and thus is a factor of 1.12 larger than for the present conditions.

For the mock-up tests a small ratio between input beam waist w_0 and waveguide width a of $w_0/a = 0.28$ was chosen. This is not optimum with respect to beam divergence, however, it does strongly reduce the risk of arcing at the waveguide entrance and in the mitre bends. By careful optimization of the input beam with respect to width and amplitude profile, a relative reduction of the beam divergence can be obtained. Limits are imposed by truncation of the input beam at the window and waveguide entrance (reflections!) as well as at the waveguide exit.

8.2 Ohmic loss

Assuming a similar corrugation profile and similar surface roughness, the absorption factor for a single reflection scales as $1/\sqrt{\sigma\lambda}$, where σ is the material conductivity and λ is the wavelength.
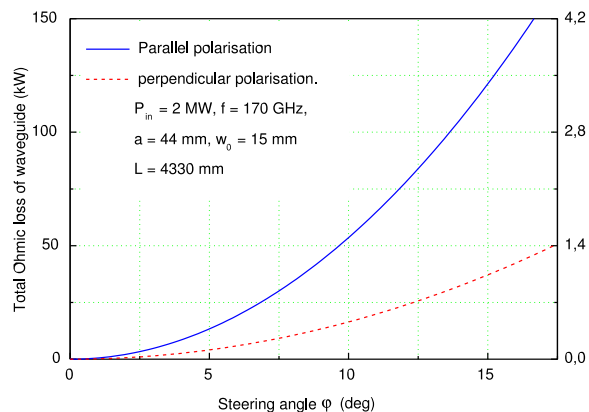

Figure 21: Expected overall ohmic loss and peak heat load of the waveguide wall in both polarisations for the ITER RS launcher at 2 MW input power

The total loss of the waveguide scales with the number of reflections from the wall, i.e., is proportional to $4a\tan\phi/\lambda$ (This expression derived from simple geometric considerations was compared with exact solutions of the field distribution on the wall and was found to be a very good approximation, See Cap. 4.1). In Fig. 21, the expected overall ohmic loss in both polarisations for the ITER RS launcher is calculated, where a conductivity of the Aluminium alloy used for the mock-up waveguide of 26 MS/m, a conductivity of copper at 200°C of 34 MS/m, and a wavelength ratio of 1.08 has been used. In the same graph, the peak power wall loading for the first reflection is plotted, where an input beam with $w_0 = 15$ mm as is foreseen at present was assumed.

At the maximum steering angle of $\phi = 12°$, a total ohmic loss of 4 % is expected in the worst case (parallel polarisation) with a maximum wall loading of 2.3 MW/m^2. Note, that the operation of the upper launcher will be with elliptical polarisation, i.e. a mixture of parallel and perpendicular polarisation.

8.3 Mitre bends

The use of mitre bends in the upper launcher of ITER is possible, however, a few percent of extra loss must be taken into account. The strong heating of the waveguide wall in the mitre bends can be handled, but should be avoided as far as possible. One means is the positioning of the bends at places where the field strength on the wall is low. A first analysis of the problem shows, that the loss of the bends can be reduced if mitre bends with higher deflections angles are used. This leads to less rotation of the polarization and thus to a lower diffraction loss. Moreover, the depth of the grooves in the mitre bends can be reduced (cf. eq. 3) and therefore, the ohmic loss is reduced as well. Additional investigations are needed to further optimize the mitre bends along these guidelines.

8.4 Arcing in the waveguide

The tests of the mock-up were performed under atmospheric conditions, using a waveguide with rectangular corrugation profile (originally not designed for high-power). As ITER will operate the launcher under vacuum and will use a rounded corrugation profile, the

arcing limits should be much higher. Therefore arcing problems for ITER conditions appear not be a major problem provided that collection of dust in the grooves of the waveguide is avoided.

9 Summary

High power tests of the remote steering launcher were performed at 140 GHz at the ECRH facility at IPP Greifswald. Although the waveguide was manufactured only for low power tests, high power tests could be successfully performed under atmospheric pressure for the straight setup. The far field patterns confirmed earlier low power measurements resulting in a usable steering range of $-12° < \phi < 12°$. The absorption coefficients for a single reflection calculated from the temperature increase of the waveguide wall agree well with the low power measurements. From the values for one reflection, an estimation of the overall ohmic losses was performed. The results confirm and supplement experiments at JAERI [14] performed on a evacuated waveguide at 170 GHz. No major obstacles were identified so far for the application on ITER, even at a 2 MW level.

References

[1] H. Zohm, Proc. of the 13th Joint Workshop on ECE and ECRH, May 2004, Nizhny Novgorod, Russia, http://www.ec13.iapras.ru/

[2] W. Kasparek, G. Gantenbein, B. Plaum, R. Wacker, A.V. Chirkov, G.G. Denisov, S.V. Kuzikov, K. Ohkubo, F. Hollmann, D. Wagner: Performance of a remote steering antenna for ECRH/ECCD applications in ITER using four-wall corrugated square waveguide. Nucl. Fusion 43 (2003), 1505 - 1512.

[3] L. Semenov, A. Rivlin, Transmission of images through optical waveguides, Laser Focus (Feb 1981), 82 - 84

[4] T. Verhoeven et.al., Proc. of the 13th Joint Workshop on ECE and ECRH, May 2004, Nizhny Novgorod, Russia, http://www.ec13.iapras.ru/

[5] Erckmann, V. et al.: The W7-X project: Scientific basis and technical realization. Proc. 17th IEEE/NPSS Symposium on Fusion Engineering, San Diego, USA (1997). Ed. IEEE, Piscataway, NJ 1998, 40 - 48.

[6] Dammertz, G. et al. : Development of a 140 GHz, 1 MW continuous wave gyrotron for the W7-X stellarator, IEEE Trans. Plasma Science, PS-30 (2002), 808 - 818.

[7] Kasparek, W. et al., in "Strong Microwaves in Plasmas 1999", ed. A.G. Litvak, Inst. of Applied Physics, Nizhny Novgorod (1999), 185 - 204.

[8] A.Bruschi et.al., Nucl. Fusion 43 (2003) 1513-1519.

[9] K. Ohkubo, S. Kubo, T. Shimozuma, H. Idei, Y. Yoshimura, T. Notake and W. Kasparek: Extension of steering angle in a square corrugated waveguide antenna. Fusion Eng. Des. 65 (2003) 657 – 672.

[10] Kasparek, W., A. Fernandez, F. Hollmann, and R. Wacker: Measurement of ohmic loss of metallic reflectors at 140 GHz by a 3-mirror resonator technique. Int. J. Infrared and Millimeter Waves 22 (2001) 1695-1707.

[11] Gantenbein, G., et al.: High-power tests of a remote-steering launcher mock-up at 140

GHz. Proc. of the 13th Joint workshop on ECE and ECRH (EC-13), Nizhny Novgorod, May 2004.

[12] G.G. Denisov, S.V. Kuzikov, and N. Kobayashi, RF analysis of ITER remote steering antenna for electron-cyclotron plasma heating "Int. J. Infrared and Millimeter Waves, 22 (2001), 1735-1760"

[13] Y. Kok and N.J. Gallagher, "Relative phases of electromagnetic waves diffracted by a perfectly conducting rectangular-grooved grating". J. Opt. Soc. A, 5 (1988), 65-73.

[14] K. Takahashi, C. Moeller et al., "High power experiments of remote steering launcher for electron cyclotron heating and current drive", Fusion Eng. Design 65 (2003) 589-598.